

1 **Tropopause Evolution in a Rapidly Intensifying Tropical Cyclone: A Static**  
2 **Stability Budget Analysis in an Idealized, Axisymmetric Framework**

3 Patrick Duran\* and John Molinari

4 *University at Albany, State University of New York, Albany, NY*

5 \**Corresponding author address:* Department of Atmospheric and Environmental Sciences, Univer-  
6 sity at Albany, State University of New York, 1400 Washington Avenue, Albany, NY.

7 E-mail: pduran2008@gmail.com

## ABSTRACT

8 Large changes in tropopause-layer static stability are observed during the  
9 rapid intensification (RI) of an idealized, axisymmetric tropical cyclone (TC).  
10 Over the eye, static stability near the tropopause decreases and the cold-point  
11 tropopause height rises by up to 4 km at the storm center. Outside of the eye,  
12 static stability increases considerably just above the cold-point tropopause,  
13 and the tropopause remains near its initial level.

14 A budget analysis reveals that the advection term, which includes differen-  
15 tial advection of potential temperature and direct advection of static stability,  
16 is important throughout the upper troposphere and lower stratosphere. Within  
17 the eye, differential advection plays a particularly important role in destabi-  
18 lizing the layer near and above the cold-point tropopause. Outside of the eye,  
19 the upper-tropospheric outflow layer exports high potential temperature ( $\theta$ )  
20 air from the eyewall to large radii in the upper troposphere. This increase in  
21  $\theta$  forces stabilization below the outflow jet and destabilization above. Vertical  
22 wind shear above and below the outflow maximum induces vertical gradi-  
23 ents of turbulence, which also modify the vertical stability profile. Mean-  
24 while, radiative heating tendencies at the top of the cirrus canopy generally  
25 act to destabilize the upper troposphere and stabilize the lower stratosphere.  
26 These turbulent and radiative processes combine to play an important role in  
27 the development of the strong stable layer immediately above the cold-point  
28 tropopause during RI.

## 29 1. Introduction

30 Using a high-resolution dropsonde dataset collected during the Tropical Cyclone Intensity Ex-  
31 periment (TCI; Doyle et al. 2017), Duran and Molinari (2018) observed dramatic changes in  
32 tropopause structure during the rapid intensification (RI) of Hurricane Patricia (2015). The goal of  
33 the present paper is to analyze the processes that might have produced the upper-tropospheric and  
34 lower-stratospheric fluctuations observed in Patricia using an idealized axisymmetric simulation.

35 After undergoing a remarkably rapid intensification (RI), Hurricane Patricia (2015) set a new  
36 record as the strongest tropical cyclone (TC) ever observed in the Western Hemisphere (Kimber-  
37 lain et al. 2016; Rogers et al. 2017). TCI dropsonde observations collected during this RI period  
38 revealed dramatic changes in the cold-point tropopause height and upper-level static stability (Du-  
39 ran and Molinari 2018). In particular, when Patricia was at tropical storm intensity shortly before  
40 RI commenced, a strong inversion layer existed just above the cold-point tropopause. During the  
41 first half of the RI period, this inversion layer weakened throughout Patricia’s inner core, with the  
42 weakening most pronounced over the developing eye. By the time the storm reached its maximum  
43 intensity of  $95 \text{ m s}^{-1}$ , the inversion layer over the eye had disappeared almost completely, which  
44 was accompanied by a greater than 1-km increase in the tropopause height. Meanwhile over the  
45 eyewall region, the static stability increased and the tropopause remained near its initial level.

46 Despite the importance of tropopause-layer thermodynamics in theoretical models of hurri-  
47 canes (Emanuel and Rotunno 2011; Emanuel 2012), most observational studies of the upper-  
48 tropospheric structure of TCs are decades old<sup>1</sup>. Recently, however, Komaromi and Doyle (2017)  
49 found that stronger TCs tended to have a higher and warmer tropopause over their inner core than  
50 weaker TCs. Their results are consistent with the evolution observed over the inner core of Hur-

---

<sup>1</sup> An in-depth review of these papers can be found in Duran and Molinari (2018).

51 ricane Patricia, in which the tropopause height increased and the tropopause temperature warmed  
52 throughout RI (Duran and Molinari 2018).

53 An idealized simulation of a TC analyzed by Ohno and Satoh (2015) suggested that the devel-  
54 opment of an upper-level warm core near the 13-km level acted to decrease the static stability near  
55 the tropopause within the eye. During the early stage of development in their simulation, large  
56 static stability existed above 16 km at all radii (their Fig. 9c). However, after the storm's inten-  
57 sification, the static stability within the eye above 16 km was markedly smaller (their Fig. 10c).  
58 Although the mechanisms that might drive this static stability evolution have not been examined  
59 explicitly, it might be related to the development of an upper-tropospheric warm core within the  
60 eye.

61 Stern and Zhang (2013) described the development of the TC warm core using a potential tem-  
62 perature ( $\theta$ ) budget analysis. Although the warm anomaly in their simulation maximized in the  
63 mid-levels, they noted that a secondary warming maximum also existed in the 12-14-km layer.  
64 Radial and vertical advection both played important roles in this warm core development through-  
65 out RI, and subgrid-scale diffusion became particularly important during the later stage of RI.  
66 The warming of the upper troposphere by these advective and diffusive processes could decrease  
67 the vertical  $\theta$  gradient, thereby contributing to a decrease in static stability near the tropopause  
68 within the eye.

69 Outside of the eye, in the presence of cirrus clouds, vertical gradients of radiative heating also  
70 can modify the tropopause-layer static stability. Bu et al. (2014) noted the existence of a shallow  
71 region of diurnal-mean net radiative cooling at the top of the TC cirrus canopy (see their Figs. 5,  
72 11). This shallow region of cooling could act to destabilize the layer just below the top of the cirrus  
73 canopy and stabilize the layer immediately above. If the top of the cirrus canopy lies close to the

74 tropopause, these radiative processes could contribute to a stabilization of the lower stratosphere,  
75 as was observed in Hurricane Patricia.

76 To our knowledge, the only paper that has examined explicitly the static stability evolution  
77 in a modeled TC is Kepert et al. (2016), but their analysis was limited to the boundary layer.  
78 The analysis herein is based upon that of Stern and Zhang (2013), except using a static stability  
79 budget similar to that of Kepert et al. (2016), with a focus on the upper-tropospheric and lower-  
80 stratospheric evolution during RI.

## 81 **2. Model Setup**

82 The numerical simulations were performed using version 19.4 of Cloud Model 1 (CM1) de-  
83 scribed in Bryan and Rotunno (2009). The equations of motion were integrated on a 3000-km-  
84 wide, 30-km-deep axisymmetric grid with 1-km horizontal and 250-m vertical grid spacing. The  
85 computations were performed on an  $f$ -plane at 15°N latitude, over a sea surface with constant  
86 temperature of 30.5°C, which matches that observed near Hurricane Patricia (2015; Kimberlain  
87 et al. 2016). Horizontal turbulence was parameterized using the Smagorinsky scheme described  
88 in Bryan and Rotunno (2009, pg. 1773), with a prescribed mixing length that varied linearly from  
89 100 m at a surface pressure of 1015 hPa to 1000 m at a surface pressure of 900 hPa. Vertical  
90 turbulence was parameterized using the formulation of Markowski and Bryan (2016, their Eq.  
91 6), using an asymptotic vertical mixing length of 100 m. A Rayleigh damping layer was applied  
92 outside of the 2900-km radius and above the 25-km level to prevent spurious gravity wave reflec-  
93 tion at the model boundaries. Microphysical processes were parameterized using the Thompson  
94 et al. (2004) scheme, and radiative heating tendencies were computed every two minutes using the  
95 Rapid Radiative Transfer Model for GCMs (RRTMG) longwave and shortwave schemes (Iacono  
96 et al. 2008). The initial temperature and humidity field was horizontally homogeneous and deter-

mined by averaging all Climate Forecast System Reanalysis (CFSR) grid points within 100 km of Patricia's center of circulation at 18 UTC 21 October 2015. The vortex described in Rotunno and Emanuel (1987, their Eq. 37) was used to initialize the wind field, setting all parameters equal to the values used therein.

Although hurricanes simulated in an axisymmetric framework tend to be more intense than those observed in nature, the intensity evolution of this simulation matches reasonably well with that observed in Hurricane Patricia. After an initial spin-up period of about 20 hours, the modeled storm (Fig. 1, blue lines) began an RI period that lasted approximately 18 hours. After this RI, the storm continued to intensify more slowly until the maximum 10-m wind speed reached  $89 \text{ m s}^{-1}$  and the sea-level pressure reached its minimum of 846 hPa 81 hours into the simulation. Hurricane Patricia (red stars) exhibited a similar intensity evolution prior to its landfall, with an RI period leading to a maximum 10-m wind speed of  $95 \text{ m s}^{-1}$  and a minimum sea-level pressure of 872 hPa.

### 3. Budget Computation

The static stability can be expressed as the squared Brunt-Väisälä frequency:

$$N_m^2 = \frac{g}{T} \left( \frac{\partial T}{\partial z} + \Gamma_m \right) \left( 1 + \frac{T}{R_d/R_v + q_s} \frac{\partial q_s}{\partial T} \right) - \frac{g}{1 + q_t} \frac{\partial q_t}{\partial z}, \quad (1)$$

where  $g$  is gravitational acceleration,  $T$  is temperature,  $R_d$  and  $R_v$  are the gas constants of dry air and water vapor, respectively,  $q_s$  is the saturation mixing ratio,  $q_t$  is the total condensate mixing ratio, and  $\Gamma_m$  is the moist-adiabatic lapse rate:

$$\Gamma_m = g(1 + q_t) \left( \frac{1 + L_v q_s / R_d T}{c_{pm} + L_v \partial q_s / \partial T} \right), \quad (2)$$

where  $L_v$  is the latent heat of vaporization and  $c_{pm}$  is the specific heat of moist air at constant pressure. In the tropopause layer,  $q_s$ ,  $\partial q_s / \partial T$ , and  $\partial q_t / \partial z$  approach zero. In this limiting case,

Eq. 1 reduces to:

$$N^2 = \frac{g}{\theta} \frac{\partial \theta}{\partial z}, \quad (3)$$

where  $\theta$  is the potential temperature.

To compute  $N^2$ , CM1 uses Eq. 1 in saturated environments and Eq. 3 in sub-saturated environments. For simplicity, however, only Eq. 3 will be employed for the budget computations throughout the entire domain<sup>2</sup>.

Taking the time derivative of Eq. 3 yields the static stability tendency:

$$\frac{\partial N^2}{\partial t} = \frac{g}{\theta} \frac{\partial}{\partial z} \frac{\partial \theta}{\partial t} - \frac{g}{\theta^2} \frac{\partial \theta}{\partial z} \frac{\partial \theta}{\partial t}, \quad (4)$$

where the potential temperature tendency,  $\partial \theta / \partial t$ , can be written, following Bryan (cited 2018):

$$\frac{\partial \theta}{\partial t} = -u \frac{\partial \theta}{\partial r} - w \frac{\partial \theta}{\partial z} + HTURB + VTURB + MP + RAD + DISS \quad (5)$$

Each term on the right-hand side of Eq. 5 represents a  $\theta$  budget variable, each of which is output directly by the model every minute.

The first term on the right-hand side of Eq. 4 is larger than the second term throughout most of the tropopause layer (not shown). Consequently, the contribution of each of the terms in Eq. 5 to the  $N^2$  tendency can be interpreted in light of a vertical gradient of each term.

Taking the vertical gradient of the first two terms on the right-hand side of Eq. 5 yields the time tendency of the vertical  $\theta$  gradient due to horizontal and vertical advection<sup>3</sup>:

$$\left( \frac{\partial}{\partial t} \frac{\partial \theta}{\partial z} \right)_{adv} = -u \frac{\partial}{\partial r} \frac{\partial \theta}{\partial z} - w \frac{\partial}{\partial z} \frac{\partial \theta}{\partial z} - \frac{\partial u}{\partial z} \frac{\partial \theta}{\partial r} - \frac{\partial w}{\partial z} \frac{\partial \theta}{\partial z}. \quad (6)$$

The first two terms on the right-hand side of Eq. 6 represent advection of static stability by the radial and vertical wind, respectively. These terms act to rearrange the static stability field, but

<sup>2</sup>The validity of this approximation will be substantiated later in this section.

<sup>3</sup>These terms include the tendencies due to implicit diffusion in the fifth-order finite differencing scheme, which are separated from the advection

cannot strengthen or weaken static stability maxima or minima. The third and fourth terms on the right-hand side of Eq. 6 represent, respectively, the tilting of isentropes in the presence of vertical wind shear, and the stretching or squashing of isentropes by vertical gradients of vertical velocity. Since these terms involve velocity gradients, they can act to strengthen or weaken static stability maxima or minima through differential advection. Unless otherwise stated, any reference to "advection" in this paper indicates the sum of all of the terms in Eq. 6.

Returning to Eq. 5, HTURB and VTURB are the  $\theta$  tendencies from the horizontal and vertical turbulence parameterizations, MP is the tendency from the microphysics scheme, RAD is the tendency from the radiation scheme, and DISS is the tendency due to turbulent dissipation. This equation neglects Rayleigh damping, since the entire analysis domain lies outside of the regions where damping is applied. Each term in Eq. 5 is substituted for  $\partial\theta/\partial t$  in Eq. 4, yielding the contribution of each budget term to the static stability tendency. These terms are summed, yielding an instantaneous "budget change" in  $N^2$  every minute. The budget changes are then averaged over 24-hour periods and compared to the total model change in  $N^2$  over that same time period, i.e.:

$$\Delta N_{budget}^2 = \frac{1}{\delta t} \sum_{t=t_0}^{t_0+\delta t} \frac{\partial N^2}{\partial t} \bigg|_t \quad (7)$$

$$\Delta N_{model}^2 = N_{t_0+\delta t}^2 - N_{t_0}^2 \quad (8)$$

$$Residual = \Delta N_{model}^2 - \Delta N_{budget}^2 \quad (9)$$

where  $t_0$  is an initial time and  $\delta t$  is 24 hours.

Eqs. 7-9 are plotted for three consecutive 24-hour periods in Fig. 2. For this and all subsequent radial-vertical cross sections, a 1-2-1 smoother is applied once in the radial direction to eliminate  $2\Delta r$  noise that appears in some of the raw model output and calculated fields. The left column of Fig. 2 depicts the model changes computed using Eq. 8, together with Eq. 1 in saturated environments and Eq. 3 in subsaturated environments. The center column depicts the budget changes



154 computed using Eq. 7 together with Eq. 3 throughout the entire domain. Thus, the left column  
155 includes the effect of moisture in the  $N^2$  computations, whereas the center column neglects mois-  
156 ture. The right column depicts the residuals, computed using Eq. 9 (i.e. the left column minus  
157 the center column.) In every 24-hour period, the budget changes are nearly identical to the model  
158 changes, which is reflected in the near-zero residuals in the right column. This indicates that the  
159 budget accurately represents the model variability, which implies that the neglect of moisture in  
160 the budget computation introduces negligible error within the analysis domain<sup>4</sup>.

161 In the tropopause layer, some of the budget terms are small enough to be ignored. To determine  
162 which of the budget terms are most important, a time series of the contribution of each of the  
163 budget terms in Eq. 5 to the tropopause-layer static stability tendency is plotted in Fig. 3. For this  
164 figure, each of the budget terms is computed using the method described in Section 3, except with  
165 1-hour averaging intervals instead of 24-hour intervals. The absolute values of these tendencies  
166 are then averaged over the radius-height domain of the plots shown in Fig. 2 and plotted as a time  
167 series<sup>5</sup>. Advection (Fig. 3, red line) plays an important role in the mean tropopause-layer static  
168 stability tendency at all times, and vertical turbulence (Fig. 3, blue line) and radiation (Fig. 3, dark  
169 green line) also contribute significantly. The remaining three processes - horizontal turbulence,  
170 microphysics, and dissipative heating - are negligible everywhere outside of the eyewall, and do  
171 not play important roles in the mesoscale tropopause variability.

172 The preceding analysis indicates that, at all times, three budget terms dominate the tropopause-  
173 layer static stability tendency: advection, vertical turbulence, and radiation. Variations in the

---

<sup>4</sup>This is not the case in the lower- and mid-troposphere, where the residual actually exceeds the budget tendencies in many places, likely due to the neglect of moisture; thus we limit this analysis to the upper troposphere and lower stratosphere.

<sup>5</sup>It will be seen in subsequent figures that each of the terms contributes both positively and negatively to the  $N^2$  tendency within the analysis domain. Thus, taking an average over the domain tends to wash out the positive and negative contributions. To circumvent this problem, the absolute value of each of the terms is averaged.

174 magnitude and spatial structure of these terms drive the static stability changes depicted in Fig. 2;  
175 subsequent sections will focus on these variations and what causes them.

## 176 **4. Results**

### 177 *a. Static stability evolution*

178 The average  $N^2$  over the first day of the simulation (Fig. 4a) indicates the presence of a weak  
179  $N^2$  maximum just above the cold-point tropopause. Over the subsequent 24 hours, during the  
180 RI period, the  $N^2$  within and above this layer decreased within the 25-km radius (Fig. 4b). This  
181 decreasing  $N^2$  corresponded to an increase in the tropopause height within the developing eye,  
182 maximized at the storm center. Outside of the eye, meanwhile, the tropopause height decreased  
183 over the eyewall region (25-60-km radius) and increased only slightly outside of the 60-km ra-  
184 dius. In this outer region, the  $N^2$  maximum just above the tropopause strengthened during RI.  
185 These trends continued as the storm's intensity leveled off in the 48-72-hour period (Fig. 4c). The  
186 tropopause height increased to nearly 21 km at the storm center and sloped sharply downward to  
187 16.3 km on the inner edge of the eyewall, near the 30 km radius. Static stability outside of the eye,  
188 meanwhile, continued to increase just above the cold-point tropopause. This  $N^2$  evolution closely  
189 follows that observed in Hurricane Patricia (2015; Duran and Molinari 2018, see their Fig. 4). The  
190 mechanisms that led to these  $N^2$  changes will be investigated in the subsequent sections.

### 191 *b. Static stability budget analysis*

#### 192 *(i) 0-24 hours*

193 The initial spin-up period was characterized by a steady increase of the maximum wind speed  
194 from 11 m s<sup>-1</sup> to 22 m s<sup>-1</sup> (Fig. 1a, blue line), an intensification rate that closely matched that of  
195 TC Patricia (Fig. 1a, red stars). The weakening of the lower-stratospheric static stability maximum

196 during this period is reflected in the total  $N^2$  budget change over this time (Fig. 5a). The layer just  
 197 above the cold-point tropopause was characterized by decreasing  $N^2$  (purple shading), maximizing  
 198 at the storm center. At and immediately below the tropopause, meanwhile,  $N^2$  increased during  
 199 this time period (green shading). Although these tendencies extended out to the 200-km radius,  
 200 they were particularly pronounced at innermost radii. A comparison of the contributions of advec-  
 201 tion (Fig. 5b), vertical turbulence (Fig. 5c), and radiation (Fig. 5d) reveals that advection was the  
 202 primary driver of the  $N^2$  tendency during this period, acting to stabilize near and just below the  
 203 tropopause and destabilize above. Although vertical turbulence acted in opposition to advection  
 204 (i.e. it acted to stabilize regions that advection acted to destabilize), the magnitude of the advec-  
 205 tive tendencies was larger, particularly at the innermost radii. The sum of advection and vertical  
 206 turbulence (Fig. 5e) almost exactly replicated the static stability tendencies above the tropopause.  
 207 Radiative tendencies, meanwhile, (Fig. 5d) acted to destabilize the layer below about 16 km and  
 208 stabilize the layer between 16 and 17 km. The sum of advection, vertical turbulence, and radiation  
 209 (Fig. 5f) reproduced the total change in  $N^2$  almost exactly.

## 210 (ii) 24-48 hours

211 During the RI period, the maximum wind speed increased from  $22 \text{ m s}^{-1}$  to  $80 \text{ m s}^{-1}$  (Fig. 1a).  
 212 Over this time,  $N^2$  within the eye generally decreased above 16 km and increased below (Fig. 6a),  
 213 with the destabilization above 16 km maximizing near the level of the mean cold-point tropopause.  
 214 These tendencies at the innermost radii were driven almost entirely by advection (Fig. 6b). Vertical  
 215 turbulence (Fig. 6c) and radiation (Fig. 6d) contributed negligibly to the static stability tendencies  
 216 in this region.

217 Outside of the eye, the  $N^2$  evolution exhibited alternating layers of positive and negative tenden-  
 218 cies. Near and above 18 km existed an upward-sloping region of decreasing  $N^2$  that extended out

219 to the 180-km radius. In this region, neither vertical turbulence nor radiation exhibited negative  $N^2$   
 220 tendencies; advection was the only forcing for this destabilization. Immediately below this layer,  
 221 just above the cold-point tropopause, was a region of increasing  $N^2$  that sloped upward from 17  
 222 km near the 30-km radius to just below 18 km outside of the 100-km radius. Advection and verti-  
 223 cal turbulence both contributed to this positive  $N^2$  tendency, with advection playing an important  
 224 role below about 17.5 km and and turbulence playing an important role above. The sum of advec-  
 225 tion and turbulence (Fig. 6e) reveals two separate regions of increasing  $N^2$  in the 17-18-km layer  
 226 rather than one contiguous region. The addition of radiation to these two terms, however, (Fig. 6f)  
 227 provides the link between these two regions, indicating that radiation also plays a role in strength-  
 228 ening the stable layer just above the tropopause. In the 16-17-km layer, just below the cold-point  
 229 tropopause, a horizontally-extensive layer of destabilization also was forced by a combination of  
 230 advection, vertical turbulence, and radiation. The sum of advection and vertical turbulence ac-  
 231 counts for only a portion of the decreasing  $N^2$  in this layer, and actually indicates forcing for  
 232 stabilization near the 50-km radius and outside of the 130-km radius. Radiative tendencies over-  
 233 come this forcing for stabilization in both of these regions to produce the radially-extensive region  
 234 of destabilization observed just below the tropopause.

235 The sum of advection, vertical turbulence, and radiation (Fig. 6f) once again closely follows  
 236 the observed  $N^2$  variability, except in the eyewall region, where the neglect of latent heating and  
 237 horizontal turbulence introduces some differences.

### 238 (iii) 48-72 hours

239 After the storm's maximum wind speed leveled off near  $80 \text{ m s}^{-1}$  (Fig. 1a), the magnitude of  
 240 the static stability tendencies within the eye decreased to near zero (Fig. 7a). Outside of the eye,  
 241 however,  $N^2$  continued to decrease in the layer immediately surrounding the tropopause and in-

crease just above. The sum of advection and vertical turbulence (Fig. 7e) indicates that these two processes account for most of the destabilization near the tropopause and some of the stabilization near the 18-km altitude. Below the tropopause, however, these two terms provided strong forcing for stabilization that was not observed in the budget change (Fig. 7a). Radiation (Fig. 7d), which generally forced stabilization above 17 km and destabilization below, balanced out this forcing for stabilization in the upper troposphere. In the eyewall region (30-80-km radius), advection and vertical turbulence combined to force destabilization in the 17-18-km layer (Fig. 7e), which was not observed in the budget change (Fig. 7a). Radiation provided strong forcing for stabilization, which outweighed this effect and produced net stabilization in a portion of this region. Outside of the 80-km radius, both advection (Fig. 7b) and vertical turbulence (Fig. 7c) provided forcing for stabilization near and just above the 18-km level. The sum of the two terms (Fig. 7e) indicates increasing  $N^2$  near the 18-km level everywhere outside of the 80-km radius, but this stabilization is slightly weaker in the 90-120-km radial band than the observed value. The addition of radiation (Fig. 7f) provided the extra forcing for stabilization required to account for the observed increase in  $N^2$ . Outside of the 120-km radius, the region of radiative forcing for stabilization sloped downward, and the increase in  $N^2$  observed near 18 km can be explained entirely by a combination of advection and vertical turbulence.

## 5. Discussion

### *a. The role of advection*

Advection played an important role in the tropopause-layer  $N^2$  evolution at all stages of intensification, but for brevity, this section will focus only on the RI (24-48-hour) period. To investigate the advective processes more closely, the individual contributions of horizontal and vertical advection

during the RI period are shown in Fig. 8, along with the corresponding time-mean radial and vertical velocities and  $\theta$ . The  $N^2$  tendencies due to the two advective components (Fig. 8a,b) exhibited strong cancellation, consistent with flow that was nearly isentropic. There existed, however, a large region near the tropopause in which the total advective tendency was nonzero (Fig. 6b). These nonzero tendencies were related to the development of the TC's secondary circulation as the storm intensified.

During the RI period, strong radial and vertical circulations developed near the tropopause (Fig. 8c,d), which forced high-magnitude  $N^2$  tendencies due to advection (Fig. 8a,b). A layer of strong outflow formed at and below the tropopause during this period, with the outflow maximum (dashed cyan line) curving from the 14-km level at the 50-km radius to just below the 16-km level outside of the 80-km radius (Fig. 8c). Notably, the  $N^2$  tendency due to horizontal advection (Fig. 8a) tended to switch signs at this line, with stabilization below the outflow maximum and destabilization above. This is consistent with the outflow layer carrying air with increasingly large  $\theta$  from the eyewall to large radii as the storm intensified. This increase in  $\theta$  maximized near the outflow maximum, which acted to decrease  $\partial\theta/\partial z$  above the outflow maximum and increase it below. This mechanism is the same as that discussed in Trier and Sharman (2009), in which vertical wind shear in the outflow layer of a mesoscale convective system modified the upper-tropospheric static stability through differential advection of isentropes.

Meanwhile in the lower stratosphere, a thin layer of 2-4 m s<sup>-1</sup> inflow developed a few hundred meters above the tropopause, similar to that which was observed in Hurricane Patricia (2015; Duran and Molinari 2018) and in previous modeling studies (e.g. Ohno and Satoh 2015; Kieu et al. 2016). Since the isentropes in this layer sloped slightly upward with radius (i.e.  $\partial\theta/\partial r < 0$ ), this inflow acted to import lower  $\theta$  air from outer radii to inner radii. Since the negative  $\theta$  tendencies

287 maximized at the level of maximum inflow, the layer below the inflow maximum destabilized and  
288 the layer above stabilized (Fig. 8a).

289 Curiously, horizontal advection contributed to the  $N^2$  tendency everywhere within the eye,  
290 even though the mean radial velocity there was near zero. Close examination of the model out-  
291 put revealed that these tendencies were forced by advective processes associated with inward-  
292 propagating waves. Although the radial velocity perturbations induced by these waves averaged  
293 out to zero, the advective tendencies forced by the radial velocity perturbations did not. Addition-  
294 ally, when these waves reached  $r=0$ , a dipole of vertical velocity resulted, with ascent above and  
295 descent below. For reasons that remain unclear, the regions of ascent were more persistent than the  
296 regions of descent, which resulted in the mean ascent observed near  $r=0$  above 17 km in Fig. 8d.

297 Vertical advection also played an important role in the tropopause-layer static stability evolution.  
298 Within the eye, subsidence dominated below 17 km, while mean ascent existed near the storm  
299 center above 17 km. Although the magnitude of the subsidence was larger at lower altitudes,  
300  $\partial\theta/\partial z$  was smaller there. Because  $\partial\theta/\partial z$  was smaller, the subsidence at lower levels could not  
301 accomplish as much warming as the subsidence at higher levels in the eye, consistent with the  
302 results of Stern and Zhang (2013). As a result, vertical advection within the eye stabilized the  
303 layer below 16 km during RI.

304 Outside of the 27-km radius, ascent dominated the troposphere, while a 1-1.5-km-deep layer  
305 of descent existed immediately above the tropopause. These regions of ascent and descent con-  
306 verged just above the tropopause; this convergence acted to compact the isentropes in this layer  
307 and increase the static stability. Above the lower-stratospheric subsidence maximum, meanwhile,  
308 vertical advection decreased  $N^2$ . Below the tropopause, differential vertical advection increased  
309  $N^2$  within the eyewall region and also at larger radii above the vertical velocity maximum at larger

310 radii. Outside of the eyewall and below the vertical velocity maximum, meanwhile, differential  
311 vertical advection acted to decrease  $N^2$ .

312 Comparing the  $N^2$  tendencies forced by horizontal (Fig. 8a) and vertical (Fig. 8b) advection  
313 to the total advective tendency seen in Fig. 6b reveals that horizontal advective tendencies domi-  
314 nated the troposphere, while vertical advective tendencies dominated the layer near and above the  
315 tropopause. Thus, tilting of isentropes in the vicinity of the upper-tropospheric outflow maximum  
316 appears to be the most important advective process governing the  $N^2$  tendency in the troposphere,  
317 whereas convergence of vertical velocity appears to be the most important advective process near  
318 the tropopause.

#### 319 *b. The role of radiation*

320 During the initial spin-up period (0-24 hours; Fig. 9a), convection was not deep enough to  
321 deposit large quantities of ice near the tropopause and create a persistent cirrus canopy. Due to the  
322 lack of ice particles, the radiative heating tendencies during this period (Fig. 9b) were relatively  
323 small and confined to the region above a few particularly strong, although transient, convective  
324 towers. During RI (24-48 hours), the eyewall updraft strengthened and a radially-extensive cirrus  
325 canopy developed near the tropopause (Fig. 9c). The enhanced vertical gradient of ice mixing ratio  
326 at the top of the cirrus canopy induced strong diurnal-mean radiative cooling near the tropopause  
327 (Fig. 9d). This cooling exceeded  $0.6 \text{ K h}^{-1}$  ( $14.4 \text{ K day}^{-1}$ ) in some places and sloped downward  
328 from the lower stratosphere into the upper troposphere, following the top of the cirrus canopy. A  
329 small radiative warming maximum also appeared outside of the 140-km radius below this region  
330 of cooling. These results broadly agree with those of Bu et al. (2014; see their Fig. 11a), whose  
331 CM1 simulations produced a  $0.3 \text{ K h}^{-1}$  diurnally-averaged radiative cooling at the top of the cirrus  
332 canopy and radiative warming within the cloud that maximized near the 200-km radius. This broad



333 region of radiative cooling acted to destabilize the layer below the cooling maximum and stabilize  
334 the layer above, which can be seen in Fig. 6d. The small area of net radiative heating outside of  
335 the 140-km radius enhanced the destabilization above 16 km in this region and produced a thin  
336 layer of stabilization in the 15-16-km layer.

337 After the TC's RI period completed (48-72 hours), strong radiative cooling remained near the  
338 tropopause at inner radii (Fig. 9f), sloping downward with the top of the cirrus canopy to below the  
339 tropopause at outer radii. Cooling rates exceeded  $1 \text{ K h}^{-1}$  ( $24 \text{ K day}^{-1}$ ) just above the tropopause  
340 between the 30- and 70-km radii. This value is more than three times the maximum cooling rate of  
341  $0.3 \text{ K h}^{-1}$  observed by Bu et al. (2014), a difference that is a consequence of their larger vertical grid  
342 spacing compared to that used here, along with a contribution from differing radiation schemes.  
343 To compare our results to theirs, we ran a simulation identical to that described in Section 2, except  
344 using the NASA-Goddard radiation scheme and 625-m vertical grid spacing, to match those of Bu  
345 et al. (2014). This simulation produced a maximum 24-hour-average radiative cooling rate of  $0.3$   
346  $\text{K h}^{-1}$ , which agrees with that shown in Bu et al. (2014). Another simulation using 625-m vertical  
347 grid spacing and RRTMG radiation produced 24-hour-average cooling rates of up to  $0.6 \text{ K h}^{-1}$ .  
348 This suggests that vertical grid spacing smaller than 625 m is necessary to resolve properly the  
349 radiative cooling at the top of the cirrus canopy, and that the results can be quite sensitive to the  
350 radiation scheme used.

351 Meanwhile below the tropopause, time-mean radiative warming spread from 30- to 160-km  
352 radius within the cirrus canopy. The existence of radiative cooling overlying radiative warming in  
353 this region led to radiatively-forced destabilization at and below the tropopause, as was observed  
354 in Fig. 7d. Beneath the warming layer existed a region of forcing for stabilization, while a much  
355 stronger region of forcing for stabilization existed in the lower stratosphere, above the cooling  
356 maximum.

357 The results herein suggest that, after the cirrus canopy developed, radiative heating tendencies  
358 considerably destabilized the upper troposphere and stabilized the lower stratosphere.

359 *c. The role of turbulent mixing*

360 Fig. 10 depicts the effect of turbulent mixing on the vertical  $\theta$  profile of an initially stably-  
361 stratified layer. At the initial time in this schematic,  $\theta$  is assumed to increase with height at a  
362 constant rate (Fig. 10, left panel). The imposition of turbulence (blue hatching) adjusts the  $\theta$   
363 profile within the mixed layer toward a constant value equal to the mean value of that layer in  
364 the initial state (Fig. 10, right panel). Just above and just below the mixed layer, however, the  $\theta$   
365 profile remains undisturbed. Consequently, although turbulent mixing acts to decrease  $\partial\theta/\partial z$  in  
366 the layer in which it is occurring, it actually increases  $\partial\theta/\partial z$  just below and just above the layer.  
367 Vertical gradients of turbulent mixing like those depicted here are quite important, particularly on  
368 the flanks of the upper-tropospheric outflow jet.

369 Two distinct maxima of vertical eddy diffusivity developed in the tropopause layer as the storm  
370 intensified (Fig. 11). Comparison of these turbulent regions to the  $N^2$  tendencies in Figs. 6c and  
371 7c reveals that the layers in which vertical eddy diffusivity maximized corresponded to layers of  
372 destabilization due to vertical turbulence. Just outside of these layers, however, vertical turbulence  
373 acted to increase  $N^2$ . The large vertical gradient of vertical eddy diffusivity near the tropopause  
374 played an important role in developing the lower-stratospheric stable layer during RI. These results  
375 support the hypothesized role of turbulence in setting the outflow-layer  $\theta$  stratification in Rotunno  
376 and Emanuel (1987).

## 6. Conclusions

The simulated  $N^2$  evolution shown herein closely matched that observed during the RI of Hurricane Patricia (2015). Three  $N^2$  budget terms dominated in the upper troposphere and lower stratosphere: advection, radiation, and vertical turbulence. Advection dominated within the eye, where it provided forcing for destabilization. Radiation and vertical turbulence played particularly important roles in developing the strong  $N^2$  maximum just above the cold-point tropopause during RI.

To put the  $N^2$  variability observed near the tropopause into context, Fig. 12 depicts the model change in  $N^2$  over the RI period (hours 24-48) from 0 to 21 km altitude, along with the vertical eddy diffusivity and the radiative heating rate. The largest changes in  $N^2$  occurred in a relatively shallow layer immediately surrounding the tropopause (Fig. 12a). This shallow layer also contained the largest diurnally-averaged radiative heating tendencies found anywhere in the domain (Fig. 12c). Values of vertical eddy diffusivity larger than any found outside of the boundary layer also resided in the upper troposphere (Fig. 12b). The results herein suggest that this turbulence not only develops as a response to the presence of small static stability and large vertical wind shear, as discussed by Molinari et al. (2014) and Duran and Molinari (2016), but also can actively increase the static stability in highly localized regions just above and below the mixed layers.

Since two of the most important processes contributing to the  $N^2$  variability are parameterized, and one (radiation) closely depends on yet another parameterized process (microphysics), the tropopause-layer  $N^2$  variability could be quite sensitive to the assumptions inherent to the parameterizations used. A better understanding of the microphysical characteristics of the TC cirrus canopy, its interaction with radiation, and outflow-layer turbulence is critical to understanding the tropopause-layer  $N^2$  evolution.

400 In this paper, all of the variables were averaged over a full diurnal cycle to eliminate the effects  
401 of diurnal variability and isolate the overall storm evolution. Diurnal variations in static stability  
402 near the tropopause are potentially of interest with respect to the tropical cyclone diurnal cycle,  
403 and will be the subject of future work.

404 *Acknowledgments.* We are indebted to George Bryan for his continued development and support  
405 of Cloud Model 1. We also thank Jeffrey Kepert, Robert Fovell, and Erika Navarro for helpful  
406 conversations related to this work. This research was supported by NSF grant AGS-1636799 and  
407 Office of Naval Research Grant N000141712110 as a part of the TCI Departmental Research  
408 Initiative.

## 409 **References**

- 410 Bryan, G. H., cited 2018: The governing equations for CM1. [Available online at [http://www2.mmm.ucar.edu/people/bryan/cm1/cm1\\_equations.pdf](http://www2.mmm.ucar.edu/people/bryan/cm1/cm1_equations.pdf)].
- 411
- 412 Bryan, G. H., and R. Rotunno, 2009: The maximum intensity of tropical cyclones in axisymmetric  
413 numerical model simulations. *Mon. Wea. Rev.*, **137**, 1770–1789.
- 414 Bu, Y. P., R. G. Fovell, and K. L. Corbosiero, 2014: Influence of cloud-radiative forcing on tropical  
415 cyclone structure. *J. Atmos. Sci.*, **71**, 1644–1622.
- 416 Doyle, J. D., and Coauthors, 2017: A view of tropical cyclones from above: The Tropical Cyclone  
417 Intensity (TCI) Experiment. *Bull. Amer. Meteor. Soc.*, **98**, 2113–2134.
- 418 Duran, P., and J. Molinari, 2016: Upper-tropospheric low Richardson number in tropical cyclones:  
419 Sensitivity to cyclone intensity and the diurnal cycle. *J. Atmos. Sci.*, **73**, 545–554.
- 420 Duran, P., and J. Molinari, 2018: Dramatic inner-core tropopause variability during the rapid  
421 intensification of Hurricane Patricia (2015). *Mon. Wea. Rev.*, **146**, 119–134.

422 Emanuel, K., 2012: Self-stratification of tropical cyclone outflow. Part II: Implications for storm  
 423 intensification. *J. Atmos. Sci.*, **69**, 988–996.

424 Emanuel, K., and R. Rotunno, 2011: Self-stratification of tropical cyclone outflow. Part I: Impli-  
 425 cations for storm structure. *J. Atmos. Sci.*, **68**, 2236–2249.

426 Iacono, M. J., J. S. Delamere, E. J. Mlawer, M. W. Shephard, S. A. Clough, and W. D. Collins,  
 427 2008: Radiative forcing by long-lived greenhouse gases: Calculations with the AER radiative  
 428 transfer models. *J. Geophys. Res.*, **113** (D13103).

429 Kepert, J. D., J. Schwendike, and H. Ramsay, 2016: Why is the tropical cyclone boundary layer  
 430 not ”well mixed”? *J. Atmos. Sci.*, **73**, 957–973.

431 Kieu, C., V. Tallapragada, D.-L. Zhang, and Z. Moon, 2016: On the development of double warm-  
 432 core structures in intense tropical cyclones. *J. Atmos. Sci.*, **73**, 4487–4506.

433 Kimberlain, T. B., E. S. Blake, and J. P. Cangialosi, 2016: Tropical cyclone report: Hurricane  
 434 Patricia. National Hurricane Center. [Available online at [www.nhc.noaa.gov](http://www.nhc.noaa.gov)].

435 Komaromi, W. A., and J. D. Doyle, 2017: Tropical cyclone outflow and warm core structure as  
 436 revealed by HS3 dropsonde data. *Mon. Wea. Rev.*, **145**, 1339–1359.

437 Markowski, P. M., and G. H. Bryan, 2016: LES of laminar flow in the PBL: A potential problem  
 438 for convective storm simulations. *Mon. Wea. Rev.*, **144**, 1841–1850.

439 Molinari, J., P. Duran, and D. Vollaro, 2014: Low Richardson number in the tropical cyclone  
 440 outflow layer. *J. Atmos. Sci.*, **71**, 3164–3179.

441 Ohno, T., and M. Satoh, 2015: On the warm core of a tropical cyclone formed near the tropopause.  
 442 *J. Atmos. Sci.*, **72**, 551–571.

443 Rogers, R. F., S. Aberson, M. M. Bell, D. J. Cecil, J. D. Doyle, J. Morgerman, L. K. Shay, and  
 444 C. Velden, 2017: Re-writing the tropical record books: The extraordinary intensification of  
 445 Hurricane Patricia (2015). *Bull. Amer. Meteor. Soc.*, **98**, 2091–2112.

446 Rotunno, R., and K. A. Emanuel, 1987: An air-sea interaction theory for tropical cyclones. Part II:  
 447 Evolutionary study using a nonhydrostatic axisymmetric numerical model. *J. Atmos. Sci.*, **44**,  
 448 542–561.

449 Stern, D. P., and F. Zhang, 2013: How does the eye warm? Part I: A potential temperature budget  
 450 analysis of an idealized tropical cyclone. *J. Atmos. Sci.*, **70**, 73–89.

451 Thompson, G., R. M. Rasmussen, and K. Manning, 2004: Explicit forecasts of winter precipitation  
 452 using an improved bulk microphysics scheme. Part I: Description and sensitivity analysis. *Mon.*  
 453 *Wea. Rev.*, **132**, 519–542.

454 Trier, S. B., and R. D. Sharman, 2009: Convection-permitting simulations of the environment sup-  
 455 porting widespread turbulence within the upper-level outflow of a mesoscale convective system.  
 456 *Mon. Wea. Rev.*, **137**, 1972–1990.

## 457 LIST OF FIGURES

- 458 **Fig. 1.** The maximum 10-m wind speed (top panel;  $\text{m s}^{-1}$ ) and minimum sea-level pressure (bottom  
459 panel; hPa) in the simulated storm (blue lines; plotted every minute) and from Hurricane  
460 Patricia's best track (red stars; plotted every six hours beginning at the time Patricia attained  
461 tropical storm intensity). The rapid weakening during the later stage of Patricia's lifetime  
462 was induced by landfall. . . . . 26
- 463 **Fig. 2.** Left panels: Twenty-four-hour changes in squared Brunt-Väisälä frequency ( $N^2$ ;  $10^{-4} \text{ s}^{-2}$ )  
464 computed using Eq. 8 over (top row) 0-24 hours, (middle row) 24-48 hours, (bottom row)  
465 48-72 hours. Middle Panels: The  $N^2$  change over the same time periods computed using Eqs.  
466 4-7, Right Panels: The budget residual over the same time periods, computed by subtracting  
467 the budget change (middle column) from the model change (left column). Orange lines  
468 represent the cold-point tropopause height averaged over the same time periods. . . . . 27
- 469 **Fig. 3.** Time series of the contribution of each of the budget terms to the time tendency of the  
470 squared Brunt-Väisälä frequency ( $N^2$ ;  $10^{-4} \text{ s}^{-2}$ ). For each budget term, the absolute value  
471 of the  $N^2$  tendency is averaged temporally over 1-hour periods (using output every minute),  
472 and spatially in a region extending from 0 to 200 km radius and 14 to 21 km altitude. . . . . 28
- 473 **Fig. 4.** Twenty-four-hour averages of squared Brunt-Väisälä frequency ( $N^2$ ;  $10^{-4} \text{ s}^{-2}$ ) over (a) 0-24  
474 hours, (b) 24-48 hours, (c) 48-72 hours. Orange lines represent the cold-point tropopause  
475 height averaged over the same time periods. . . . . 29
- 476 **Fig. 5.** (a) Total change in  $N^2$  over the 0-24-hour period ( $10^{-4} \text{ s}^{-2} (24 \text{ h})^{-1}$ ) and the contributions to  
477 that change from (b) the sum of horizontal and vertical advection, (c) vertical turbulence, (d)  
478 longwave and shortwave radiation, (e) the sum of horizontal advection, vertical advection,

479	and vertical turbulence, and (f) the sum of horizontal advection, vertical advection, vertical	
480	turbulence, and longwave and shortwave radiation. Green shading indicates regions of sta-	
481	bilization and purple shading indicates regions of destabilization. Orange lines represent the	
482	cold-point tropopause height averaged over the 0-24-hour period. . . . .	31
483	<b>Fig. 6.</b> As in Fig. 5, but for the 24-48-hour period. . . . .	32
484	<b>Fig. 7.</b> As in Fig. 5, but for the 48-72-hour period. . . . .	33
485	<b>Fig. 8.</b> The contributions to the change in $N^2$ over the 24-48-hour period ( $10^{-4} \text{ s}^{-2} (24 \text{ h})^{-1}$ ) by	
486	(a) horizontal advection and (b) vertical advection. (c) The radial velocity ( $\text{m s}^{-1}$ ; filled con-	
487	tours), potential temperature (K; thick black contours), cold-point tropopause height (orange	
488	line), and level of maximum outflow (dashed cyan line) averaged over the 24-48-hour period.	
489	(d) The vertical velocity ( $\text{cm s}^{-1}$ ; filled contours), potential temperature (K; thick black con-	
490	tours), and cold-point tropopause height (orange line) averaged over the 24-48-hour period.	
491	34	
492	<b>Fig. 9.</b> Ice mixing ratio ( $\text{g kg}^{-1}$ ) and cold-point tropopause height (orange lines) averaged over (a)	
493	0-24 hours, (c) 24-48 hours, and (e) 48-72 hours. Radiative heating rate ( $\text{K h}^{-1}$ ) and cold-	
494	point tropopause height (orange lines) averaged over (b) 0-24 hours, (d) 24-48 hours, and (f)	
495	48-72 hours. . . . .	36
496	<b>Fig. 10.</b> Schematic diagram of the effect of turbulent mixing on the vertical profile of potential tem-	
497	perature ( $\theta$ ). At the initial time (left panel), potential temperature is assumed to increase	
498	with height at a constant rate (thick black line). The imposition of turbulence within a por-	
499	tion of the layer (blue hatching) adjusts the potential temperature profile toward the mean	



500 initial value of that layer. After a period of mixing (right panel) the potential temperature in  
 501 the mixed layer does not vary with height, but just above and just below the mixed layer, it  
 502 rapidly increases with height. . . . . 37

503 **Fig. 11.** Vertical eddy diffusivity ( $\text{m}^2 \text{s}^{-2}$ ; filled contours), cold-point tropopause height (cyan lines),  
 504 and radial velocity ( $\text{m s}^{-1}$ ; thick black lines) averaged over (a) 0-24 hours, (b) 24-48 hours,  
 505 and (c) 48-72 hours. . . . . 38

506 **Fig. 12.** (Top panel) Change in  $N^2$  over the 24-48-hour period ( $10^{-4} \text{s}^{-2} (24 \text{ h})^{-1}$ ) directly output by  
 507 the model for the 0-21-km layer. (Middle panel) Vertical eddy diffusivity ( $\text{m}^2 \text{s}^{-2}$ ) averaged  
 508 over the same time period. (Bottom panel) Radiative heating rate ( $\text{K h}^{-1}$ ) averaged over the  
 509 same time period. . . . . 40

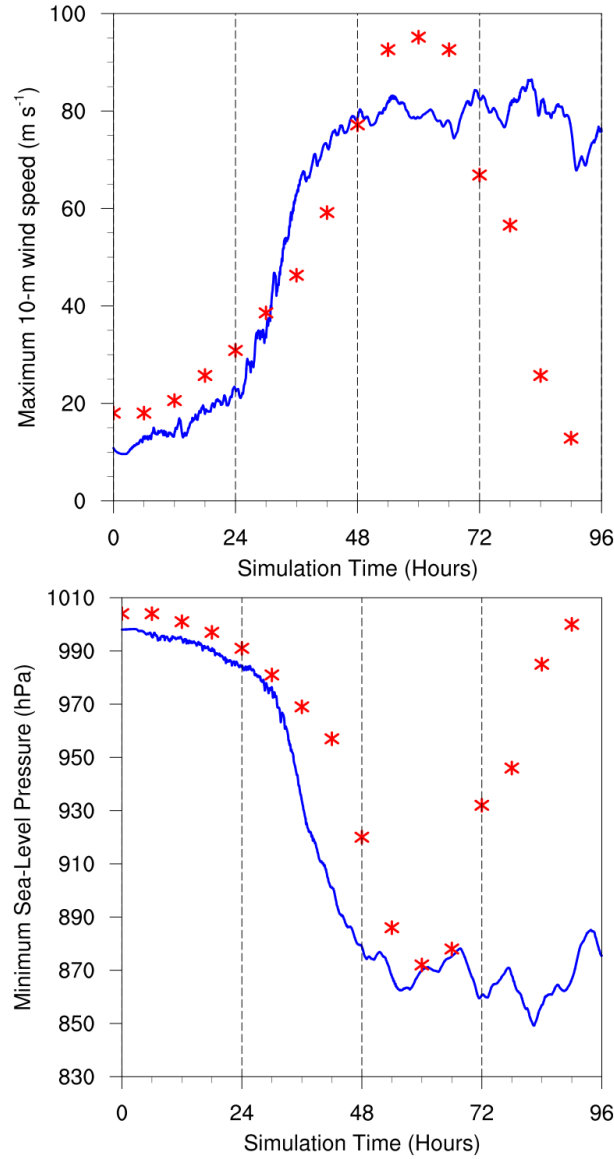


FIG. 1. The maximum 10-m wind speed (top panel;  $\text{m s}^{-1}$ ) and minimum sea-level pressure (bottom panel; hPa) in the simulated storm (blue lines; plotted every minute) and from Hurricane Patricia's best track (red stars; plotted every six hours beginning at the time Patricia attained tropical storm intensity). The rapid weakening during the later stage of Patricia's lifetime was induced by landfall.

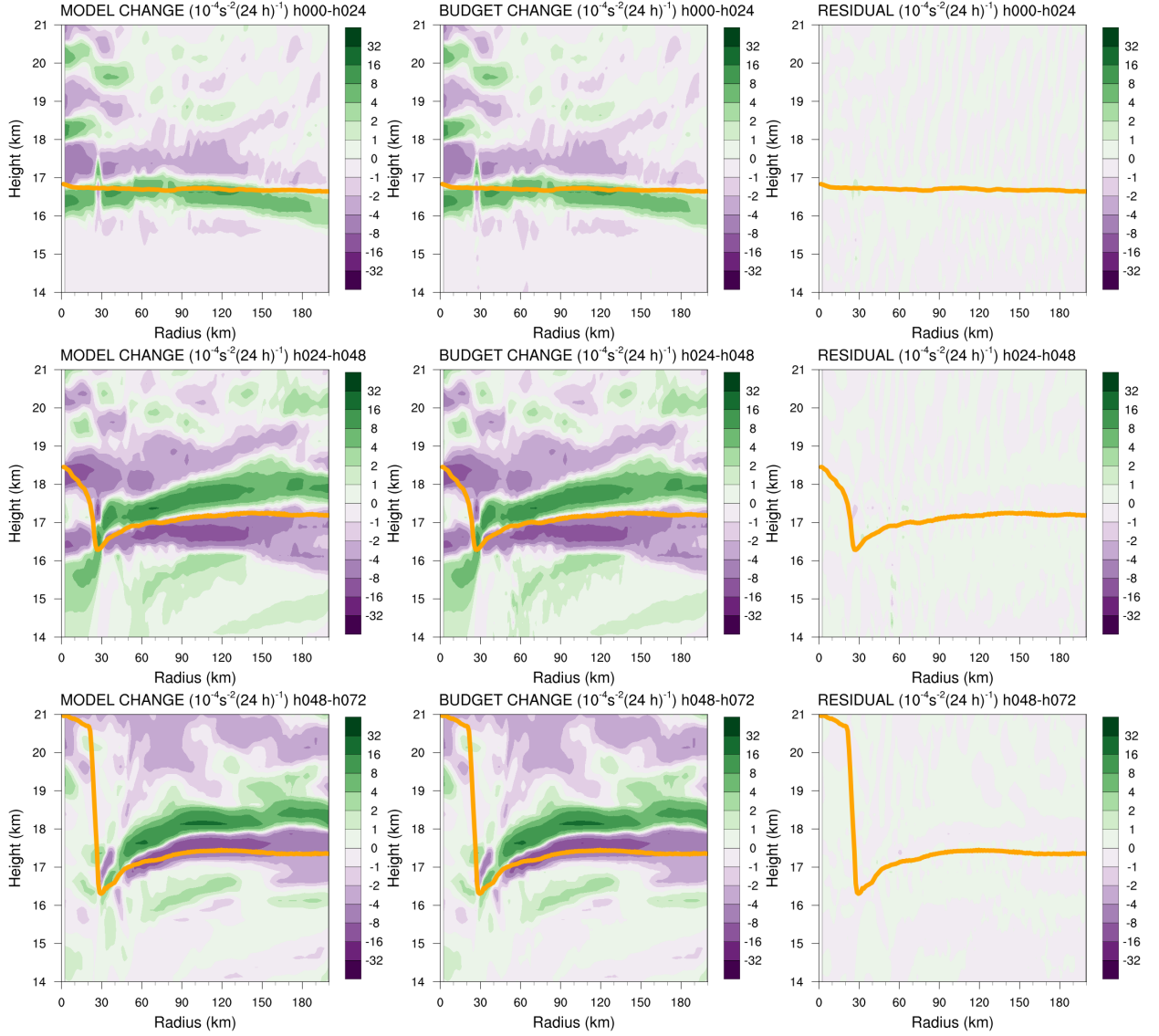


FIG. 2. Left panels: Twenty-four-hour changes in squared Brunt-Väisälä frequency ( $N^2$ ;  $10^{-4} \text{ s}^{-2}$ ) computed using Eq. 8 over (top row) 0-24 hours, (middle row) 24-48 hours, (bottom row) 48-72 hours. Middle Panels: The  $N^2$  change over the same time periods computed using Eqs. 4-7, Right Panels: The budget residual over the same time periods, computed by subtracting the budget change (middle column) from the model change (left column). Orange lines represent the cold-point tropopause height averaged over the same time periods.

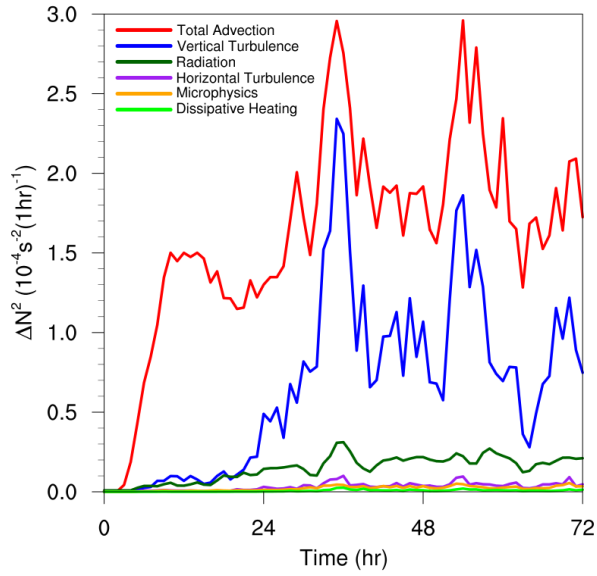


FIG. 3. Time series of the contribution of each of the budget terms to the time tendency of the squared Brunt-Väisälä frequency ( $N^2$ ;  $10^{-4} \text{ s}^{-2}$ ). For each budget term, the absolute value of the  $N^2$  tendency is averaged temporally over 1-hour periods (using output every minute), and spatially in a region extending from 0 to 200 km radius and 14 to 21 km altitude.

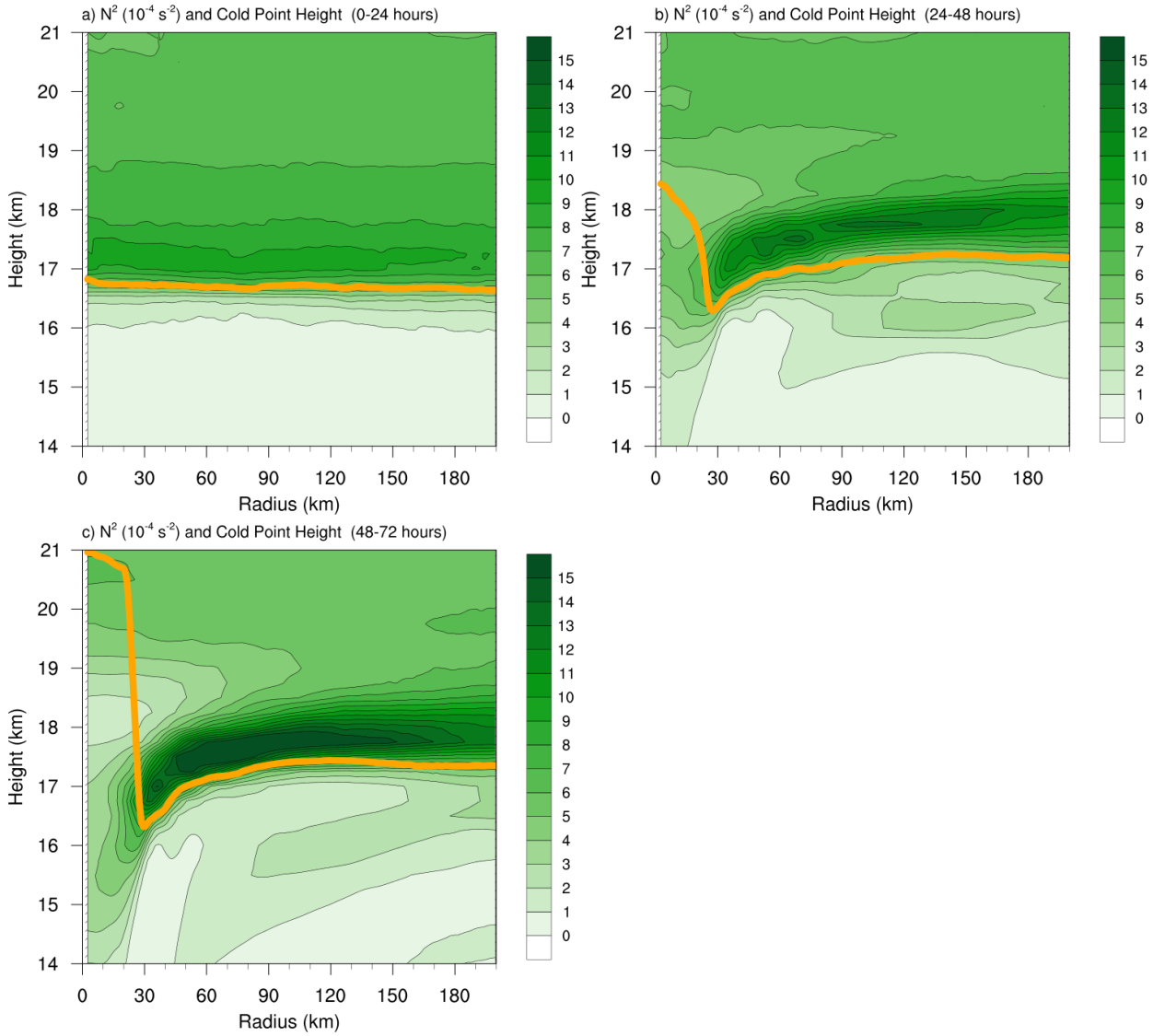
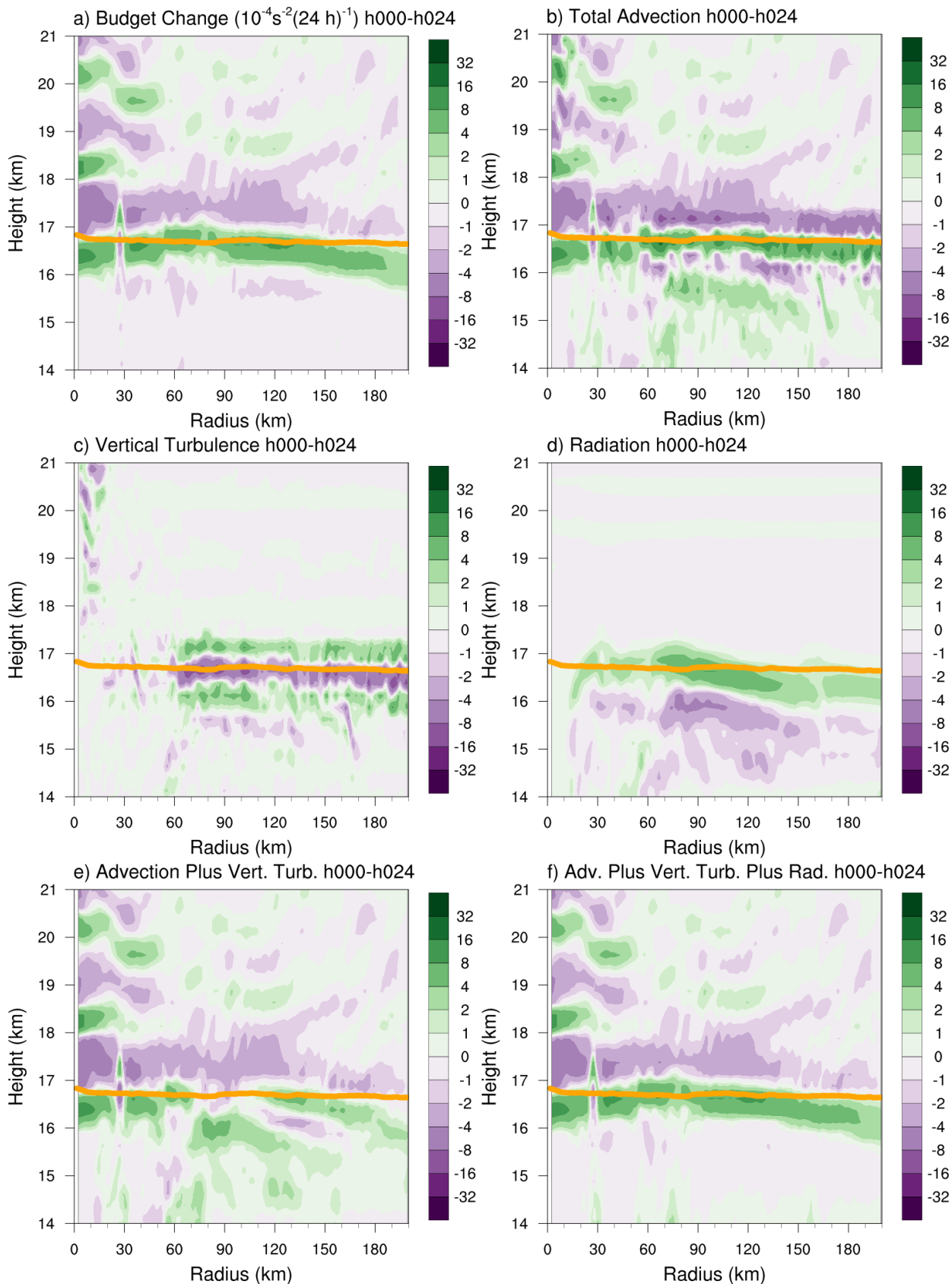


FIG. 4. Twenty-four-hour averages of squared Brunt-Väisälä frequency ( $N^2$ ;  $10^{-4} \text{ s}^{-2}$ ) over (a) 0-24 hours, (b) 24-48 hours, (c) 48-72 hours. Orange lines represent the cold-point tropopause height averaged over the same time periods.



526 FIG. 5. (a) Total change in  $N^2$  over the 0-24-hour period ( $10^{-4} \text{ s}^{-2} (24 \text{ h})^{-1}$ ) and the contributions to that change  
 527 from (b) the sum of horizontal and vertical advection, (c) vertical turbulence, (d) longwave and shortwave  
 528 radiation, (e) the sum of horizontal advection, vertical advection, and vertical turbulence, and (f) the sum of  
 529 horizontal advection, vertical advection, vertical turbulence, and longwave and shortwave radiation. Green  
 530 shading indicates regions of stabilization and purple shading indicates regions of destabilization. Orange lines  
 531 represent the cold-point tropopause height averaged over the 0-24-hour period.

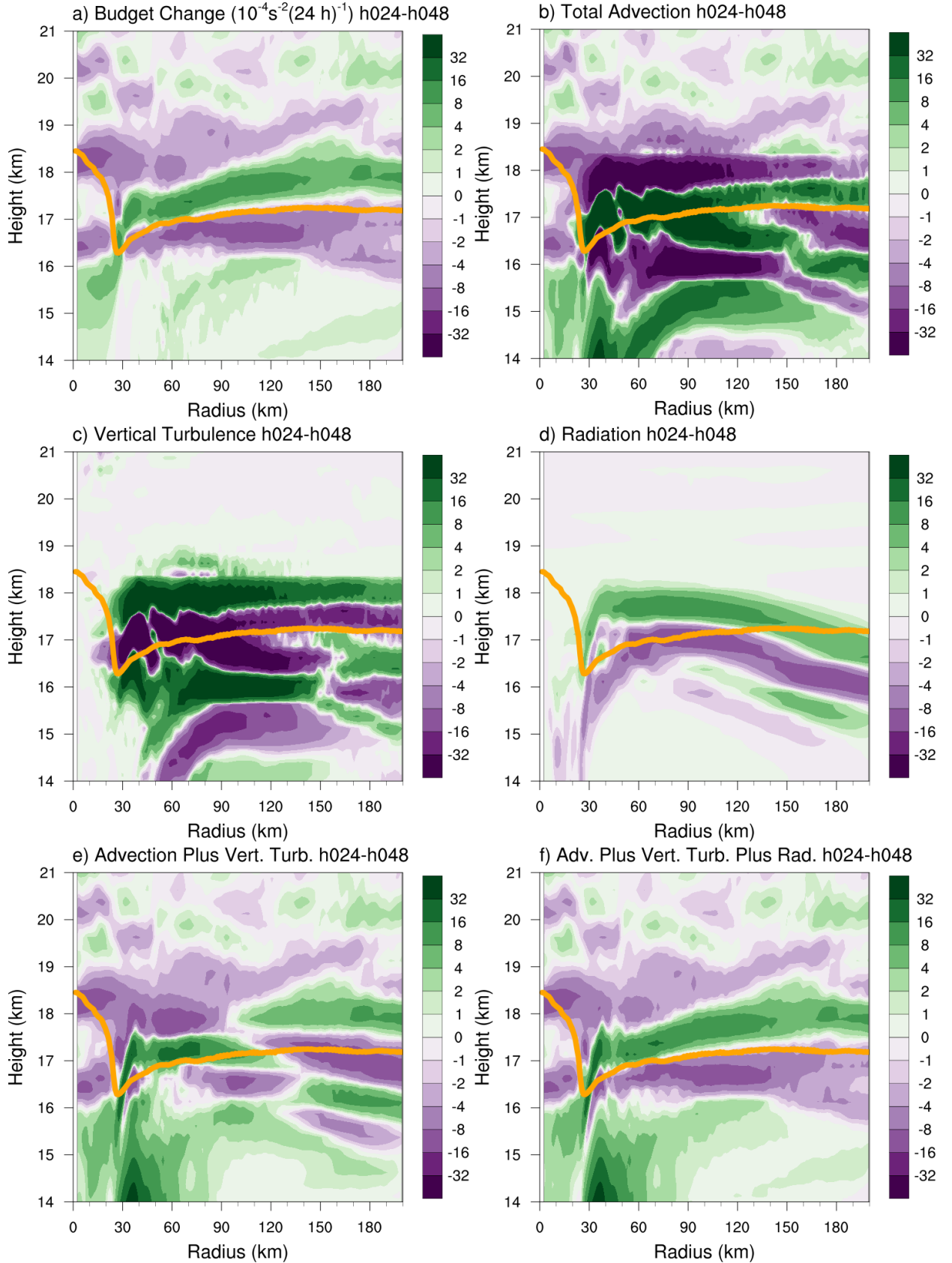


FIG. 6. As in Fig. 5, but for the 24-48-hour period.



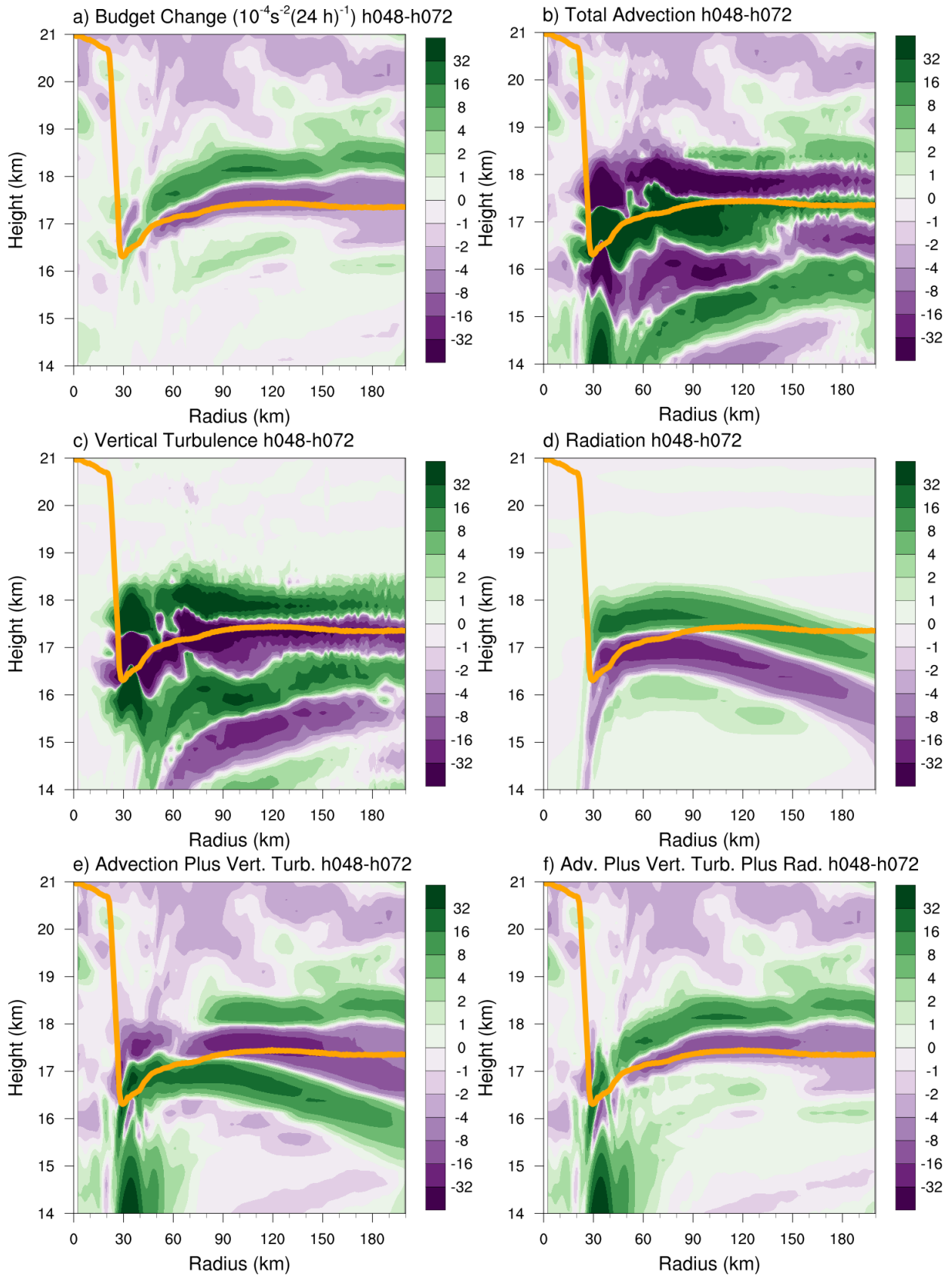


FIG. 7. As in Fig. 5, but for the 48-72-hour period.

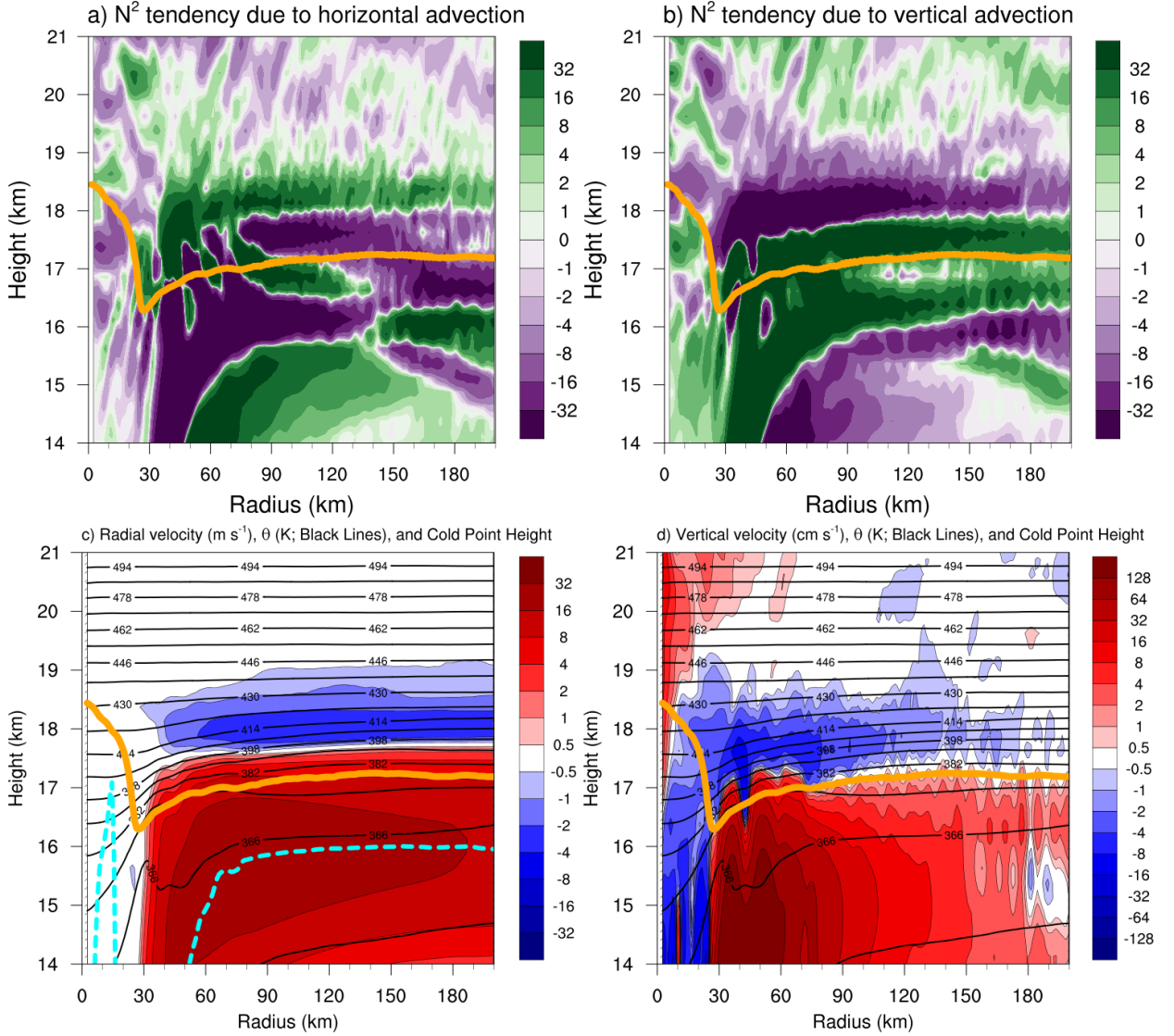
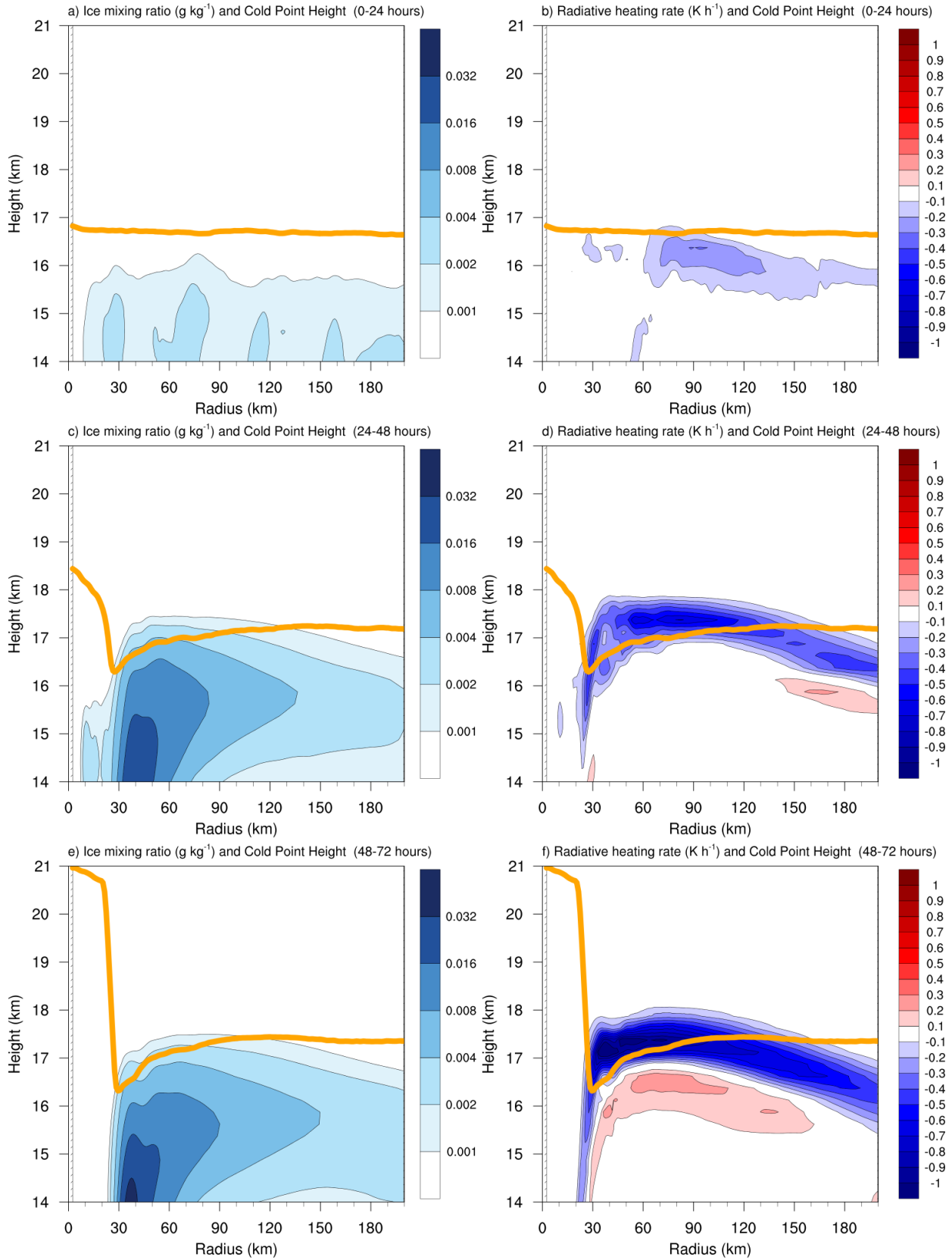


FIG. 8. The contributions to the change in  $N^2$  over the 24-48-hour period ( $10^{-4} \text{ s}^{-2} (24 \text{ h})^{-1}$ ) by (a) horizontal advection and (b) vertical advection. (c) The radial velocity ( $\text{m s}^{-1}$ ; filled contours), potential temperature ( $\text{K}$ ; thick black contours), cold-point tropopause height (orange line), and level of maximum outflow (dashed cyan line) averaged over the 24-48-hour period. (d) The vertical velocity ( $\text{cm s}^{-1}$ ; filled contours), potential temperature ( $\text{K}$ ; thick black contours), and cold-point tropopause height (orange line) averaged over the 24-48-hour period.



538 FIG. 9. Ice mixing ratio ( $\text{g kg}^{-1}$ ) and cold-point tropopause height (orange lines) averaged over (a) 0-24 hours,  
539 (c) 24-48 hours, and (e) 48-72 hours. Radiative heating rate ( $\text{K h}^{-1}$ ) and cold-point tropopause height (orange  
540 lines) averaged over (b) 0-24 hours, (d) 24-48 hours, and (f) 48-72 hours.

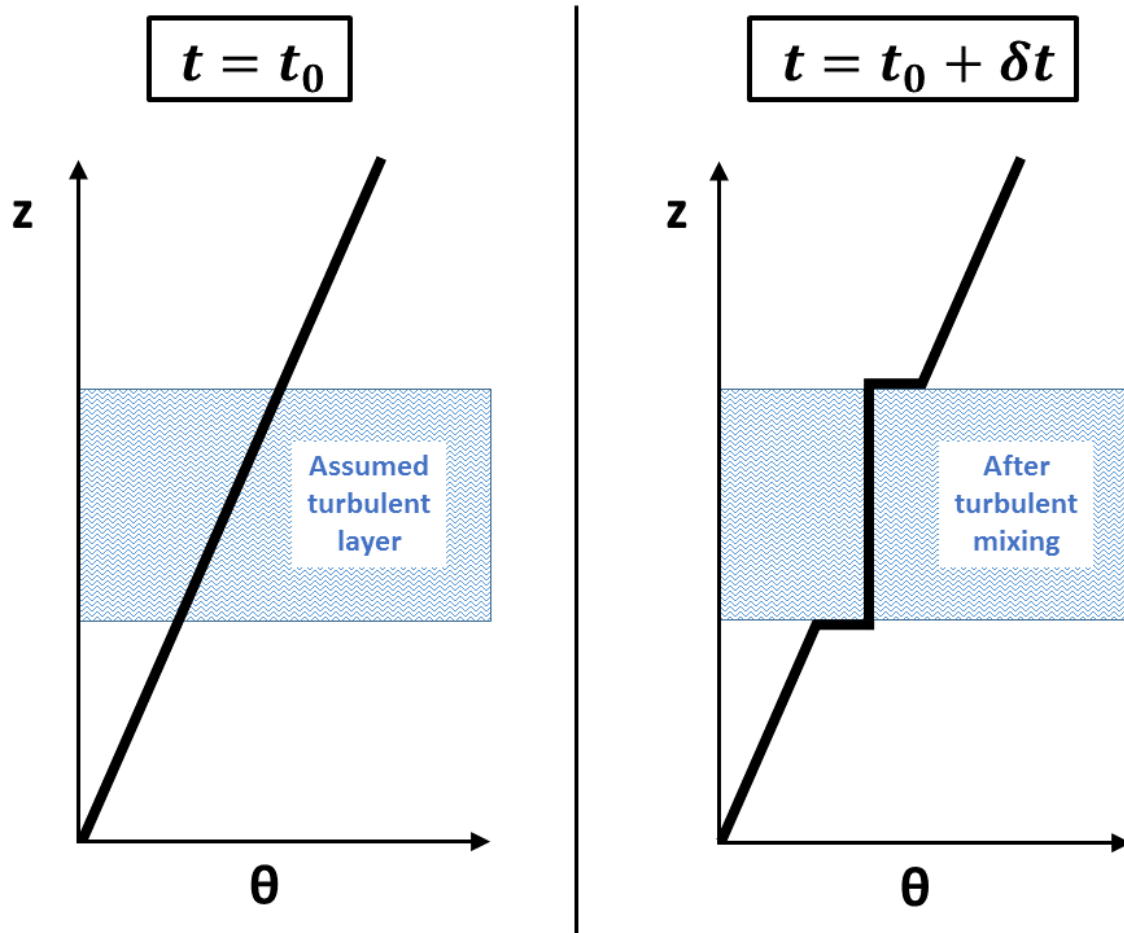


FIG. 10. Schematic diagram of the effect of turbulent mixing on the vertical profile of potential temperature ( $\theta$ ). At the initial time (left panel), potential temperature is assumed to increase with height at a constant rate (thick black line). The imposition of turbulence within a portion of the layer (blue hatching) adjusts the potential temperature profile toward the mean initial value of that layer. After a period of mixing (right panel) the potential temperature in the mixed layer does not vary with height, but just above and just below the mixed layer, it rapidly increases with height.

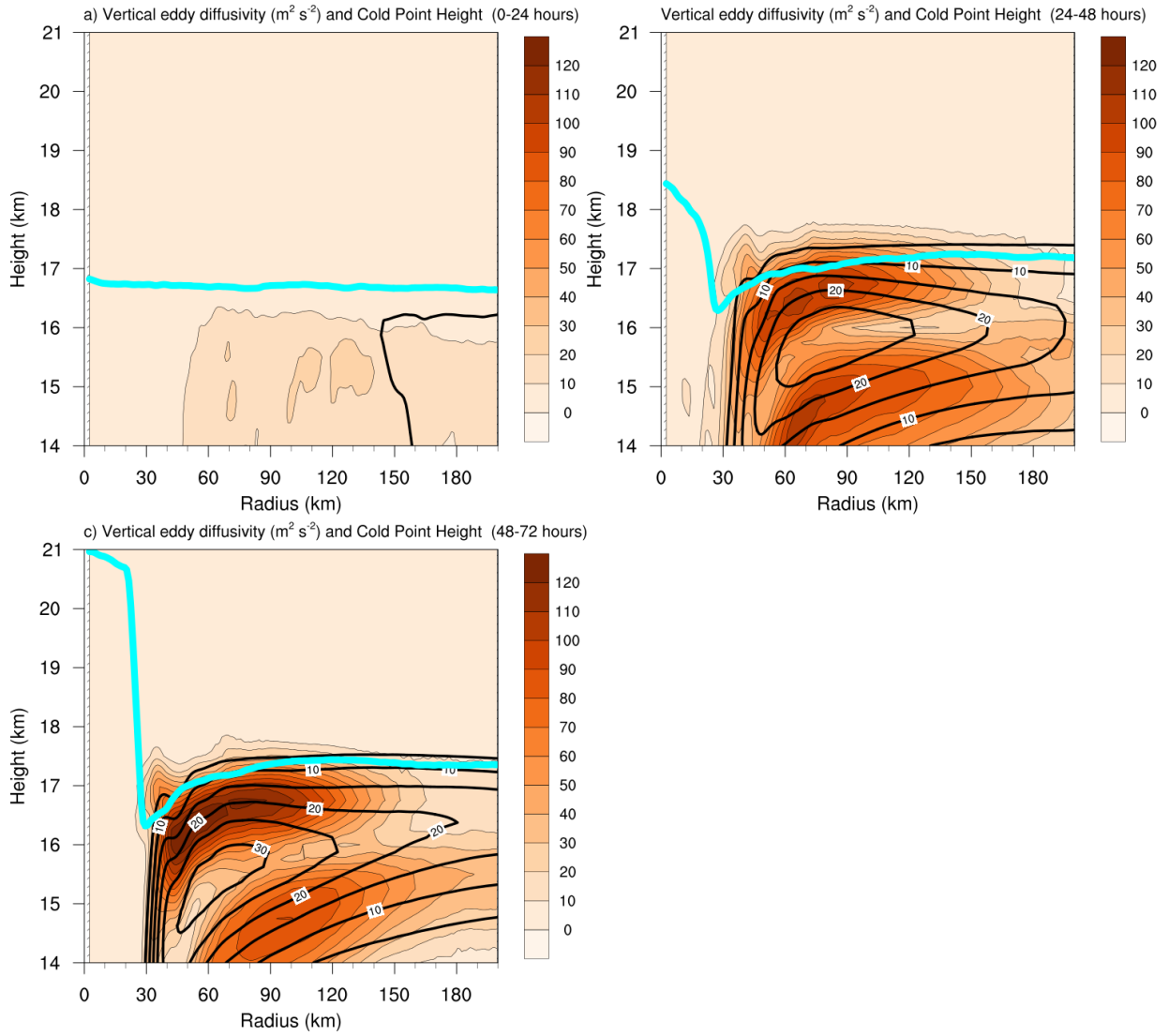
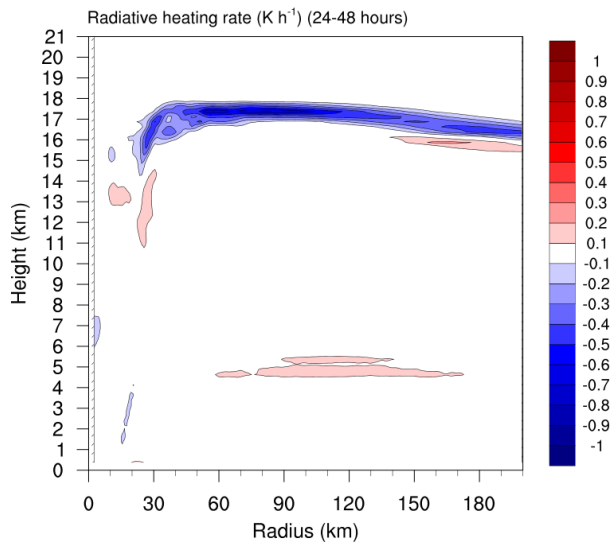
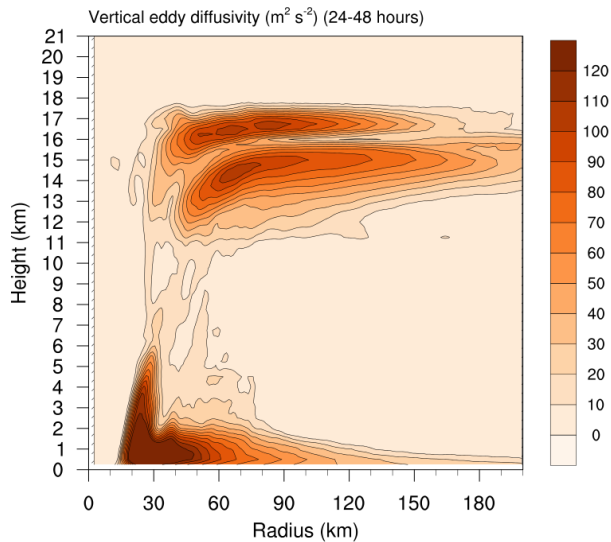
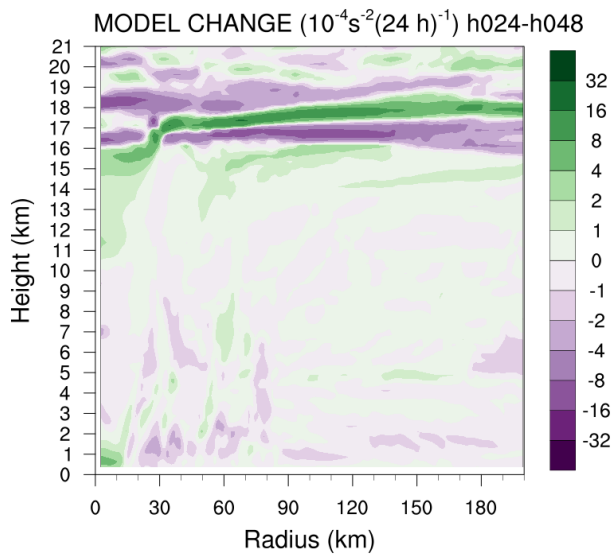


FIG. 11. Vertical eddy diffusivity ( $\text{m}^2 \text{s}^{-2}$ ; filled contours), cold-point tropopause height (cyan lines), and radial velocity ( $\text{m s}^{-1}$ ; thick black lines) averaged over (a) 0-24 hours, (b) 24-48 hours, and (c) 48-72 hours.



549 FIG. 12. (Top panel) Change in  $N^2$  over the 24-48-hour period ( $10^{-4} \text{ s}^{-2} (24 \text{ h})^{-1}$ ) directly output by the model  
550 for the 0-21-km layer. (Middle panel) Vertical eddy diffusivity ( $\text{m}^2 \text{ s}^{-2}$ ) averaged over the same time period.  
551 (Bottom panel) Radiative heating rate ( $\text{K h}^{-1}$ ) averaged over the same time period.